

Permutation blocking path integral Monte Carlo simulations of degenerate electrons at finite temperature

Tobias Dornheim* | Simon Groth | Michael Bonitz

Institut für Theoretische Physik und Astrophysik,
Christian-Albrechts-Universität zu Kiel, Kiel,
Germany

* Correspondence

Tobias Dornheim, Institut für Theoretische Physik
und Astrophysik, Christian-Albrechts-Universität
zu Kiel, Leibnizstr. 15, D-24098 Kiel, Germany.
Email: dornheim@theo-physik.uni-kiel.de

Funding Information

This research was supported by the Deutsche
Forschungsgemeinschaft, BO1366-10/2.
Norddeutscher Verbund für Hoch- und
Höchstleistungsrechnen grant shp00015.

We analyse the simulation of strongly degenerate electrons at finite temperature using the recently introduced permutation blocking path integral Monte Carlo (PB-PIMC) method [T. Dornheim et al., *New J. Phys.* **17**, 073017 (2015)]. As a representative example, we consider electrons in a harmonic confinement and carry out simulations for up to $P = 2000$ so-called imaginary-time propagators – an important convergence parameter within the PIMC formalism. This allows us to study the P -dependence of different observables of the configuration space in the Monte Carlo simulations and of the fermion sign problem. We find a surprisingly persisting effect of the permutation blocking for large P , which is explained by comparing different length scales. Finally, we touch upon the uniform electron gas in the warm dense matter regime.

KEYWORDS

degenerate electrons, path integral Monte Carlo, quantum Monte Carlo, statistical mechanics

1 | INTRODUCTION

Over the last decade, there has been a remarkable spark of interest in the properties of electrons at high densities and temperatures. This regime, which is often denoted as *warm dense matter*, is of key relevance for the description of, for example, astrophysical objects,^[1–7] hot-electron chemistry,^[8,9] and inertial confinement fusion.^[10–12] For this reason, these extreme conditions are now routinely realized at large research facilities such as the European X-FEL (free electron laser) in Germany,^[13] the Linac Coherent Light Source in Stanford^[14,15] and the National Ignition Facility at the Lawrence Livermore National Laboratory.^[16,17]

On the other hand, a rigorous theoretical description of electrons in the warm dense matter regime is considered most challenging because of the intricate and non-trivial interplay of (a) Coulomb coupling, (b) quantum degeneracy, and (c) thermal excitation effects. For this reason, *ab initio* quantum Monte Carlo (QMC) methods, which can take into account all of these effects accurately, are widely recognized as the best option. Unfortunately, path integral Monte Carlo (PIMC) simulations^[18,19] of electrons are severely limited by the notorious fermion sign problem (FSP),^[20–22] which often renders the most interesting parameter regimes inaccessible.

Consequently, over the last years there has been a surge of new developments in QMC methods at finite temperatures.^[20,23–35] In particular, the recently introduced combination of two complementary methods^[20,24–26,35,36] has made it possible to effectively avoid the sign problem and to achieve a complete description of a uniform electron gas covering the entire warm dense matter regime. On one hand side, the configuration PIMC (CPIMC) method^[23,26,37] is formulated in Fock space and can be interpreted as performing a Metropolis Monte Carlo evaluation of the exact infinite perturbation expansion around the ideal system. Hence, CPIMC is very efficient at weak non-ideality and strong degeneracy, but breaks down with increasing coupling strength. On the other hand, the permutation blocking PIMC (PB-PIMC) approach^[26,34,35] significantly extends standard PIMC towards

lower temperatures and higher densities. While it has been well known that the application of antisymmetric imaginary-time propagators (i.e., determinants)^[38–40] can lead to a reduction of the FSP, this advantage quickly vanishes with an increasing number of high-temperature factors P that are needed to reduce the factorization error in the density matrix, see Equation (4) below. Therefore, in the PB-PIMC method the determinants are combined with a higher order factorization of the density matrix,^[41,42] which allows high accuracy even for small P .

In this work, we present a detailed analysis of PB-PIMC simulations of strongly degenerate electrons at finite temperature. In section 2, we introduce the theory of standard PIMC (section 2.1), the origin of the FSP (section 2.2), and how it can be alleviated using the permutation blocking idea (section 2.3). Subsequently, we present results for electrons in a harmonic trap (section 3.1) and analyse the impact of the number of high temperature factors $P = 2, \dots, 2000$ on different expectation values and discuss the corresponding impact on the sign problem. In addition, we touch upon the uniform electron gas (section 3.2), and end with a brief summary and discussion in section 4.

2 | THEORY

2.1 | Standard path integral Monte Carlo

The standard PIMC method was introduced in the 1960s for the simulation of ^4He ^[43,44] and has subsequently emerged as one of the most powerful many-body simulation techniques at finite temperature, see Ref. [19] for a review article. More specifically, PIMC has allowed key insights to the physics of, for example, superfluidity,^[45–47] collective excitations,^[48–50] and structural properties.^[51–54] While *ab initio* simulations of up to $N = 10^4$ correlated bosons and boltzmannons (i.e., distinguishable particles obeying Boltzmann statistics) are feasible,^[55,56] PIMC simulations of fermions are severely limited by the notorious FSP,^[20–22] as we shall see in the following sections.

Let us consider a system of N particles in a fixed volume V at a temperature T in thermodynamic equilibrium. In this case, all thermodynamic observables can be computed from the canonical partition function

$$Z = \text{Tr} \hat{\rho}, \quad (1)$$

which is defined as the trace over the canonical density operator

$$\hat{\rho} = e^{-\beta \hat{H}}, \quad (2)$$

with $\beta = 1/k_B T$ being the usual inverse temperature. By restricting ourselves to distinguishable particles and evaluating Equation (1) in coordinate representation, we obtain

$$Z = \int d\mathbf{R} \langle \mathbf{R} | e^{-\beta \hat{H}} | \mathbf{R} \rangle, \quad (3)$$

where $\mathbf{R} = \{\mathbf{r}_1, \dots, \mathbf{r}_N\}$ contains the all DN particle coordinates (with D denoting the number of dimensions). Unfortunately, the matrix elements of the density operator, Equation (2), cannot be readily evaluated as the kinetic and potential parts of the Hamiltonian, \hat{K} and \hat{V} (with $\hat{H} = \hat{K} + \hat{V}$), do not commute, i.e.

$$e^{-\beta \hat{H}} \neq e^{-\beta \hat{K}} e^{-\beta \hat{V}} \quad (4)$$

To overcome this obstacle, we use the group property

$$e^{-\beta \hat{H}} = \prod_{\alpha=0}^{P-1} e^{-\varepsilon \hat{H}}, \quad (5)$$

with $\varepsilon = \beta/P$, and insert $P - 1$ unity operators of the form $\hat{1} = \int d\mathbf{R}_\alpha | \mathbf{R}_\alpha \rangle \langle \mathbf{R}_\alpha |$ into Equation (3) and obtain

$$Z = \int d\mathbf{X} \langle \mathbf{R}_0 | e^{-\varepsilon \hat{H}} | \mathbf{R}_1 \rangle \langle \mathbf{R}_1 | \dots | \mathbf{R}_{P-1} \rangle \langle \mathbf{R}_{P-1} | e^{-\varepsilon \hat{H}} | \mathbf{R}_0 \rangle \quad (6)$$

Note that Equation (6) is still exact, and the integration is carried out over P sets of particle coordinates, $d\mathbf{X} = d\mathbf{R}_0 \dots d\mathbf{R}_{P-1}$. The new expression for Z given by Equation (6) is very advantageous, as each factor appears at a P -times higher temperature. In the limit of large P , the inequality from Equation (4) disappears, and the primitive factorization becomes exact.^[57]

$$e^{-\beta \hat{H}} = \lim_{P \rightarrow \infty} (e^{-\varepsilon \hat{V}} e^{-\varepsilon \hat{K}})^P \quad (7)$$

The partition function is finally interpreted as the sum over all closed paths \mathbf{X} of particle coordinates in the so-called imaginary time $\tau \in [0, -i\hbar\beta]$:

$$Z = \int d\mathbf{X} W(\mathbf{X}), \quad (8)$$

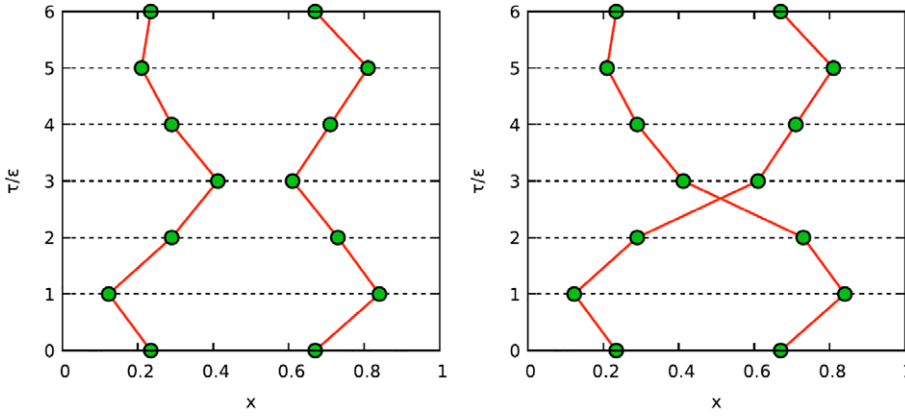


FIGURE 1 Schematic illustration of path integral Monte Carlo. Shown are two configurations in the τ - x plane with no pair-exchange (left) and a single pair exchange (right). The corresponding configuration weights are positive and negative. Reproduced from Dornheim et al.^[26] with the permission of the authors. Copyright Elsevier BV

with $W(\mathbf{X})$ denoting the corresponding configuration weight. In the left panel of Figure 1, we show such a configuration \mathbf{X} with $P=6$ and $N=2$, and each particle is represented by an entire β -periodic (i.e., closed) path in the imaginary time. The general idea of the PIMC method is to stochastically generate all paths using the Metropolis Monte Carlo scheme,^[58] which is not affected by the large number of dimensions in Equation (6).

2.2 | PIMC simulation of indistinguishable particles and the fermion sign problem

Let us now extend our consideration to the simulation of N (spin-polarized) indistinguishable particles. For this purpose, the partition function from the previous section has to be extended to include the sum over all $N!$ permutations of particle coordinates:

$$Z = \frac{1}{N!} \sum_{\sigma \in S_N} \text{sgn}^{\text{b/f}}(\sigma) \int d\mathbf{R} \langle \mathbf{R} | e^{-\beta \hat{H}} | \hat{\pi}_\sigma \mathbf{R} \rangle, \quad (9)$$

where $\hat{\pi}_\sigma$ denotes the exchange operator corresponding to the element σ from the permutation group S_N . While for bosons the sign $\text{sgn}^{\text{b}}(\sigma)$ is always 1, for fermions $\text{sgn}^{\text{f}}(\sigma)$ alternates with the number of pair exchanges. This is further illustrated in the right panel of Figure 1, where we show a configuration \mathbf{X} of two particles where the coordinates have been permuted. This results in a closed path that is periodic with respect to $\tau = 2\beta$, or, equivalently, an exchange cycle containing two particles at once. In the case of fermions, this single pair exchange leads to a negative configuration weight. Therefore, the fermionic partition function, Equation (9), constitutes a sum over both positive and negative terms, so that $W(\mathbf{X})$ can no longer be interpreted as a probability distribution, and a stochastic sampling of the paths is not directly possible.

Fortunately, the Metropolis algorithm can still be used by introducing the modified partition function

$$Z' = \int d\mathbf{X} |W(\mathbf{X})|, \quad (10)$$

and the exact fermionic expectation value can then be computed as

$$\langle O \rangle = \frac{\langle OS \rangle'}{\langle S \rangle'}, \quad (11)$$

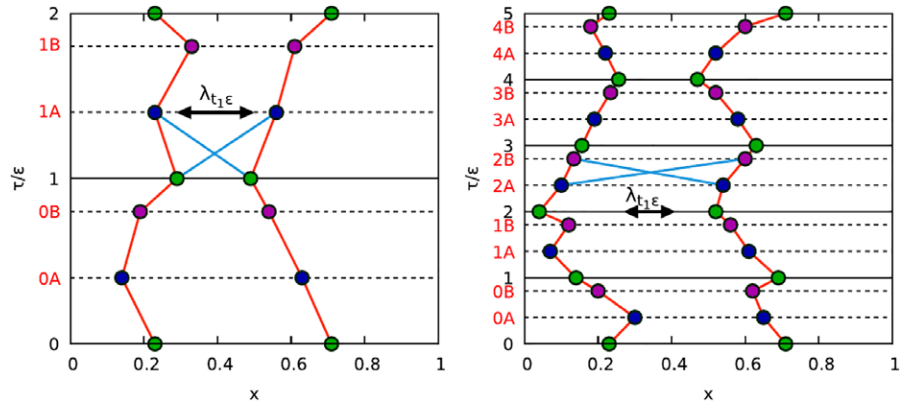
with averages being carried out over the modified distribution $W'(\mathbf{X}) = |W(\mathbf{X})|$ and $S = W(\mathbf{X})/|W(\mathbf{X})| = \text{sgn}^{\text{f}}(\sigma)$ denoting the sign. Note that, in the case of standard PIMC, this modified configuration space directly corresponds to the simulations of bosons, and all fermionic effects like Pauli blocking are realized by a subsequent cancellation of positive and negative terms in Equation (11), which is very inefficient. The average sign, that is, the denominator, is a measure for this cancellation. It can be shown that it exponentially decreases with inverse temperature and system size, $\langle S \rangle' \propto e^{-\beta N(f-f')}$, with f and f' being the free energy per particle of the original and the modified system.

The statistical uncertainty of the Monte Carlo result, ΔO , is, in first order, inversely proportional to $\langle S \rangle'^{[20]}$:

$$\frac{\Delta O}{O} \propto \frac{1}{\langle S \rangle' \sqrt{N_{\text{MC}}}} \propto \frac{e^{\beta N(f-f')}}{\sqrt{N_{\text{MC}}}} \quad (12)$$

Evidently, the error bar exponentially increases with β and N , which can only be compensated by increasing the number of Monte Carlo samples with $1/\sqrt{N_{\text{MC}}}$. In practice, this quickly becomes unfeasible, and the simultaneous vanishing of both the numerator and denominator in Equation (11) constitutes an *exponential wall*. This is the infamous FSP,^[21,22] which prohibits standard PIMC simulations even of relatively small systems at moderate temperatures.

FIGURE 2 Schematic illustration of permutation blocking path integral Monte Carlo. Shown are two configurations in the τ - x plane with $P=2$ (left) and $P=5$ (right) high temperature factors. The different colours correspond to the three different types of imaginary-time slices, and the arrows show the thermal wavelength of a single time step, $\lambda_\epsilon(P) = (2\pi\epsilon/3)^{1/2}$. The red and blue connections depict the diagonal and off-diagonal elements in the diffusion matrices, respectively. Reproduced from Dornheim et al.^[26] with the permission of the authors. Copyright Elsevier BV



2.3 | Permutation blocking path integral Monte Carlo

The permutation blocking PIMC method^[34,35] significantly extends standard PIMC simulations towards stronger quantum degeneracy as it occurs, for example, in the warm dense matter regime.^[26]

The first ingredient to this approach is the application of antisymmetric imaginary-time propagators^[38–40] (i.e., determinants), which allows us to combine permutations in Equation (9) that contribute to the partition function with a different sign. This is illustrated in the left panel of Figure 2, where we show a configuration \mathbf{X} of two particles. In standard PIMC, we either evaluate the red connections corresponding to a positive weight, or the blue connections corresponding to a pair exchange and, therefore, a negative weight. In contrast, the application of the permutation blocking allows us to combine both paths into a single meta-configuration, so that a significant part of the cancellation is carried out analytically within the determinants. There is, however, a catch: with an increasing number of high-temperature factors P , which are needed to bring down the factorization error in Equation (4), the effect of the blocking decreases, see the right panel of Figure 2. For large P , we either have large diagonal elements (no pair exchange) as in the depicted example configuration, or large off-diagonal elements, but they are never comparable at the same time. Therefore, it is crucial to combine the determinants with a higher order factorization of the density matrix that allows sufficient accuracy for small P , which constitutes the second key ingredient to the PB-PIMC method. The final result for Z is then given by

$$Z = \frac{1}{(N!)^{3P}} \int d\mathbf{X} \prod_{\alpha=0}^{P-1} \left(e^{-\epsilon \tilde{V}_\alpha} e^{-\epsilon^3 u_0 \frac{\hbar^2}{m} \tilde{F}_\alpha} \det(\rho_\alpha) \det(\rho_{\alpha A}) \det(\rho_{\alpha B}) \right), \quad (13)$$

where the \tilde{V} and \tilde{F} terms contain all contributions due to the potential energy and the forces, and we have to compute three determinants of the diffusion matrices ρ_α for every high-temperature factor. The particular definition of these functions and a detailed discussion of the employed factorization scheme^[41,42] can be found in Refs. [26, 34].

In a nutshell, by using the determinants in Equation (13), the modified weights $W(\mathbf{X})$ already contain a significant part of cancellations, which makes the modified configuration space different from the bosonic case and brings it closer to a direct sampling of fermionic configurations (in which case all terms would be positive and the FSP vanishes). The beneficial consequences of this circumstance are discussed in detail in the following section.

3 | RESULTS

3.1 | 2D harmonic trap

Let us first consider the case of N spin-polarized electrons in a harmonic confinement, which are described by a Hamiltonian of the form

$$\hat{H} = -\frac{1}{2} \sum_{k=1}^N \nabla_k^2 + \frac{1}{2} \sum_{k=1}^N \mathbf{r}_k^2 + \sum_{k<l}^N \frac{\lambda}{|\mathbf{r}_l - \mathbf{r}_k|}, \quad (14)$$

and we use oscillator units (i.e., the characteristic length $l_0 = \sqrt{\hbar/m\Omega}$ and energy scale $E_0 = \hbar\Omega$, with Ω being the trap frequency) throughout this work. Note that Equation (14) is often considered as a simple model for electrons in a quantum dot.^[59–61] In Figure 3, we show the results for $N=4$ electrons at $\beta=3$ and $\lambda=1$. The left ordinate corresponds to the average sign S , and the green crosses and red circles depict PB-PIMC and standard PIMC data, respectively, which are shown versus the inverse number of high-temperature factors P . Evidently, standard PIMC is afflicted with a severe sign problem and we find $S \sim 10^{-2}$. Note that the average sign exhibits only a very weak dependence on P , which is a consequence of the factorization error, Equation (4), but does not reflect any qualitative changes in the FSP. In stark contrast, the PB-PIMC results exhibit

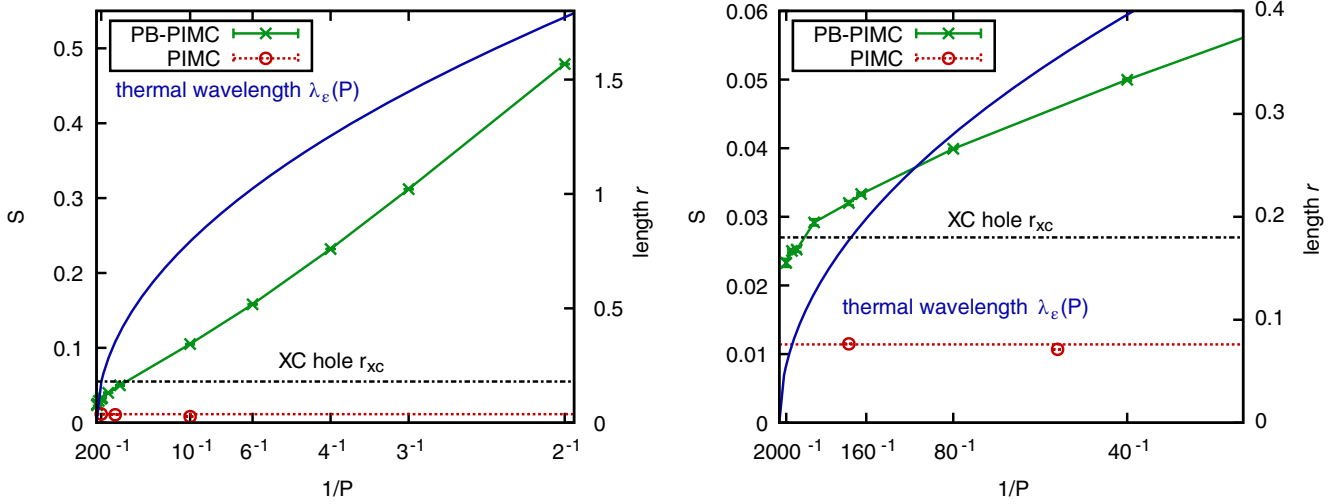


FIGURE 3 P -dependence of the average sign for PB-PIMC (green) and PIMC (red) for $N = 4$ electrons in a 2D harmonic trap at $\beta = 3$ and $\lambda = 1$. The left ordinate corresponds to the sign S and the right ordinate to a distance r in coordinate space corresponding to the XC hole r_{xc} (black) and the thermal wavelength of a single propagator, $\lambda_\epsilon(P) = (2\pi\epsilon/3)^{1/2}$ (blue). The right panel shows a magnified segment around larger numbers of high-temperature factors

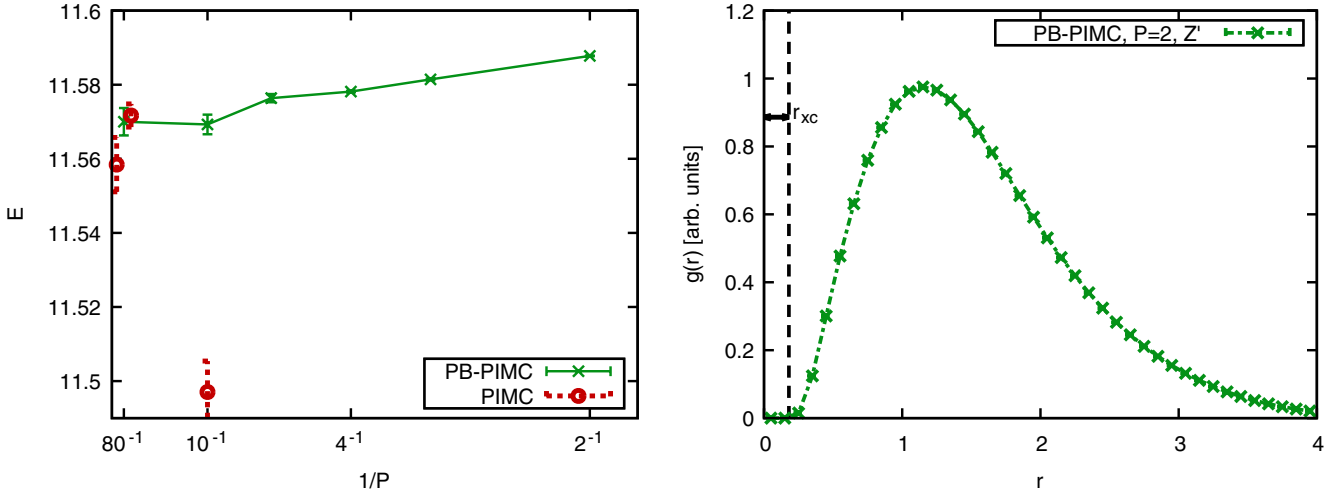


FIGURE 4 PB-PIMC and PIMC results for $N = 4$ electrons at $\beta = 3$ and $\lambda = 1$. The left panel shows the convergence of the total energy E with P , and the right panel shows the averaged pair correlation function $g(r)$ computed with PB-PIMC for $P = 2$ in the modified configuration space Z' . In addition, the arrow indicates the exchange-correlation hole r_{xc}

the expected swift decrease with increasing P , as explained in detail by Groth et al. [26]. However, at a first glance, the average sign does not seem to converge towards the value from standard PIMC, as expected from the theory, but stays considerably larger even for large P . This finding can be understood by examining the right ordinate, which corresponds to a distance r in the coordinate space. The blue curve depicts the thermal wavelength of a single step in the imaginary time, $\lambda_\epsilon(P) = (2\pi\epsilon/3)^{1/2}$, and the dash-dotted horizontal line depicts the extension of the exchange-correlation hole r_{xc} , see also Figure 4 (right panel). The increased sign in the PB-PIMC method as compared to standard PIMC is a direct consequence of the analytical permutation blocking that is carried out within the determinants in Equation (13). This effect fully disappears only when the thermal wavelength is much smaller than the smallest distance between two particles within the PB-PIMC simulation, that is, when $\lambda_\epsilon \ll r_{xc}$. Evidently, λ_ϵ slowly vanishes only for large P , and the average sign starts to exhibit a more steep decrease for $P \sim 10^3$, see also the right panel showing a magnified segment around large numbers of high-temperature factors. In summary, we have found that permutation blocking has a noticeable effect on the average sign for unexpectedly large numbers P , which is a direct consequence of the ratio of the thermal wavelength of a single high-temperature factor λ_ϵ and the exchange-correlation hole r_{xc} .

Let us next consider the convergence of a relevant observable. In the left panel of Figure 4, we show the P dependence of the total energy E both for PB-PIMC (green crosses) and standard PIMC (red circles). Observe the small error bars in the PB-PIMC data for small P , which are a direct result of the large sign. Upon increasing P , the sign drops and, consequently, the statistical uncertainty increases, see Equation (12). In addition, because of the employed higher order factorization, we observe

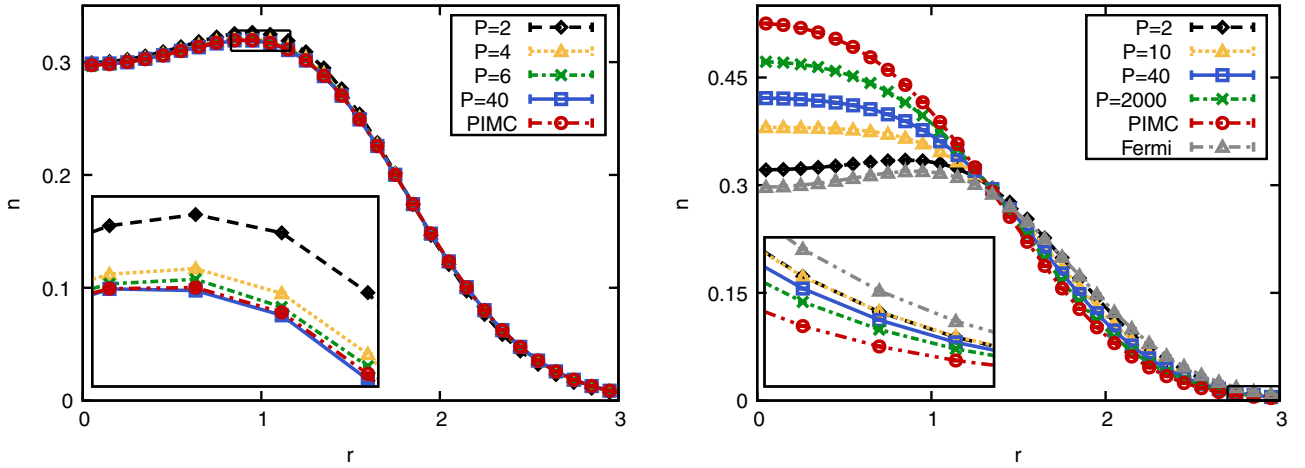


FIGURE 5 PB-PIMC and PIMC results for the radial density $n(r)$ for $N=4$ electrons at $\beta=3$ and $\lambda=1$. The left panel shows the convergence of the fermionic density, and the right panel shows the corresponding densities obtained in the modified configuration space Z' (i.e., the bosonic density in the case of standard PIMC)

a remarkably weak dependence of E on the number of high-temperature factors, and even for $P=2$ we have a relative accuracy of the order of $\Delta E/E \sim 10^{-4}$. In contrast, the standard PIMC simulations are afflicted with an equally severe sign problem independent of P , and the factorization error due to the primitive factorization, cf., Equation (4), is significantly larger.

In the right panel of Figure 4, we show PB-PIMC data for the pair distribution function

$$g(r) = \frac{1}{A} \left\langle \sum_{i=1}^N \sum_{k=i+1}^N \delta(r - r_{i,k}) \right\rangle, \quad (15)$$

with an arbitrary normalization A and the definition $r_{i,k} = |\mathbf{r}_k - \mathbf{r}_i|$. Observe that the expectation value in Equation (15) is carried out in the modified configuration space, and $g(r)$ can be divided into three distinct segments: for $r < r_{xc}$, we have the exchange-correlation hole and two particles never appear at such a small distance towards each other; around $r \approx 1$ there is a broad peak corresponding to particles located around the centre of the trap; for $r \gtrsim 2$ there is a slowly decreasing tail of particle pairs at opposite ends of the system.

Finally, in the left panel Figure 5 we show results for the radial density $n(r)$. The red circles correspond to standard PIMC results for $P=200$, which are exact within the given statistical uncertainty. The black diamonds, yellow triangles, green crosses, and blue squares correspond to the PB-PIMC results for $P=2$, $P=4$, $P=6$, and $P=40$, respectively. Again, we observe a strikingly fast convergence with P , and deviations to the PIMC data are hard to resolve with the bare eye.

In the right panel of the same figure, we show results for $n(r)$ directly evaluated in the modified configuration space, that is, the distribution of particles within a given simulation without taking into account the cancellation defined in Equation (11). In the case of standard PIMC, this corresponds to the exact bosonic density, cf., the red circles. For comparison, we have also included the fermionic density as grey triangles. As expected, bosons tend to cluster around the centre of the trap, whereas the Pauli blocking acts as an effective repellent force that pushes the electrons away from each other. Consequently, the fermionic density at $r=0$ is decreased by a factor of 40%, and the electrons are squeezed outwards. The black diamonds depict PB-PIMC results for $P=2$, which are remarkably close to the fermionic distribution. Therefore, a significant fraction of the fermionic exchange effects is captured by the determinants, the modified configuration space is close to the fermionic one, and the impact of the cancellation of positive and negative terms is small. With increasing P , there appears a progression away from the fermionic and towards the bosonic density, and, in the limit of large P , the PB-PIMC simulation will reproduce the standard PIMC simulation and the effect of the determinants will completely vanish. In practice, this means that within the QMC simulation there will only seldom appear a particle at large r , see also the inset showing a magnified segment around this regime. Therefore, the comparatively much larger values of the fermionic density can be achieved only by evaluating Equation (11) with a small average sign, which makes the simulations drastically more expensive.

3.2 | Uniform electron gas

As a second example, we consider the uniform electron gas,^[26] that is, N electrons in a box of length L and volume $V = L^3$ with periodic boundary conditions. However, since the convergence behaviour with the number of high-temperature factors P is qualitatively similar to the previously shown harmonic trap, here we restrict ourselves to a graphical interpretation of the configurations.

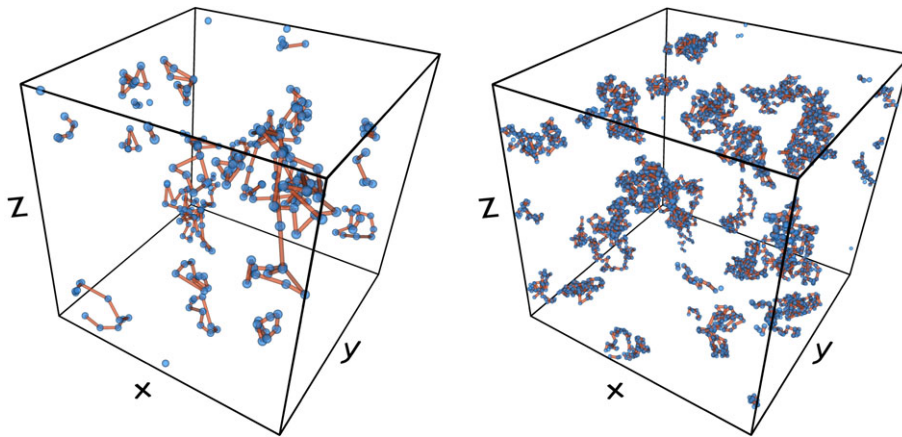


FIGURE 6 Snapshots from standard PIMC simulations of $N = 33$ spin-polarized electrons at $r_s = 1$ and $\theta = 0.75$ with $P = 9$ (left) and $P = 100$ (right)

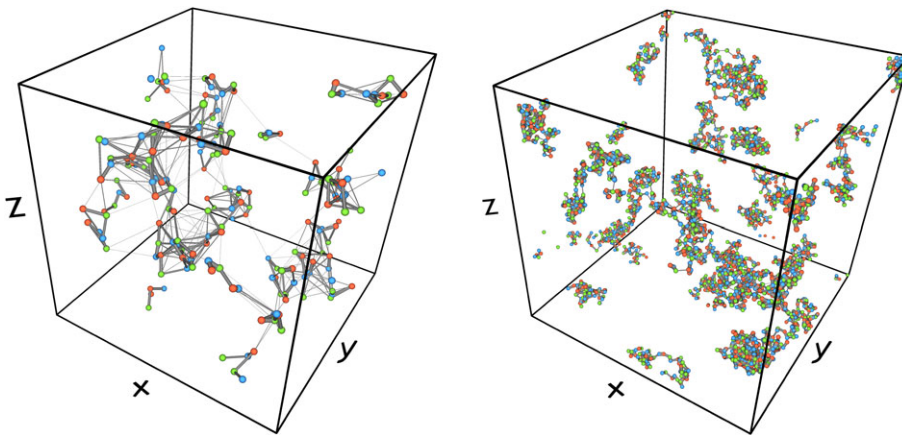


FIGURE 7 Snapshots from PB-PIMC simulations of $N = 33$ spin-polarized electrons at $r_s = 1$ and $\theta = 0.75$ with $P = 2$ (left) and $P = 30$ (right)

In Figure 6, we show snapshots from a standard PIMC simulation of $N = 33$ spin-polarized electrons at $r_s = 1$ and $\theta = 0.75$ (with the density parameter $r_s = [3V/4\pi N]^{1/3}$, the degeneracy temperature $\theta = k_B T/E_F$, and E_F denoting the Fermi energy), which corresponds to the heart of the so-called warm dense matter regime.^[26] The left panel depicts a configuration for $P = 9$ high-temperature factors, and the right panel for $P = 100$. While in the former case the paths look considerably more scrawly and less smooth than in the latter, the difference is only quantitative.

In Figure 7 we show snapshots from a PB-PIMC simulation at equal parameters. The different colours correspond to the three different types of imaginary time slices for each high-temperature factor, see section 2.3, and the width of the connections between particles is a direct measure for the associated diffusion matrix elements. For $P = 2$ (left panel), the permutation blocking is very effective, and many particles are integrated in multiple paths at the same time. Since different paths correspond to distinct permutations of particle coordinates, which enter the fermionic expectation value with different signs, the simultaneous evaluation of many such terms leads to a significant reduction of the sign problem. The right panel corresponds to $P = 30$ and, in stark contrast to the standard PIMC, the depicted configuration is qualitatively different from the $P = 2$ case. In particular, because of the decreased value of the thermal wavelength λ_e (see also Figure 3), only a few particles are involved in multiple paths with a non-vanishing weight, and the configuration resembles the smooth paths from standard PIMC shown in the right panel of Figure 6.

4 | SUMMARY AND DISCUSSION

In summary, we have presented a thorough introduction to the PIMC formalism and explained in detail the origin of the infamous sign problem in the case of fermions. In addition, we have investigated the dependence of the average sign on the number of imaginary-time propagators P , both for the standard PIMC approach and the more sophisticated PB-PIMC technique. While the sign in standard PIMC exhibits a weak P -dependence, as expected, in PB-PIMC the utilized number of propagators within the simulation crucially influences the observed sign. This is due to the decreasing effect of the analytic cancellation of configurations with different particle permutations (i.e., the eponymous permutation blocking) with increasing P , which is the major advantage of PB-PIMC. Interestingly, even for very large P this blocking effect leads to a significantly larger sign compared to standard PIMC, since the condition for an equal sign of both methods is that the

exchange-correlation hole must be significantly larger than the thermal wavelength of a single propagator; this occurs only for $P \gg 2000$.

Furthermore, we have demonstrated that both the energy and the radial density for electrons in a harmonic trap converge remarkably fast with P for PB-PIMC, which is in stark contrast standard to the primitive factorization used in standard PIMC. By further analysing the density profile, we have found that for small numbers of propagators, the PB-PIMC algorithm more closely samples the real fermionic configuration space, in accordance with the previous finding of a more efficient cancellation of configurations in this case. Lastly, we have depicted various simulations snapshots of both methods for the uniform electron gas in the warm dense matter regime, which further illustrates that the qualitative structure of the sampled paths becomes more equal with an increasing number of propagators.

We expect our results to be useful for the further development of fermionic QMC methods at finite temperature, which is of paramount importance for a variety of fields such as warm dense matter,^[26] electrons in quantum dots,^[60] ultra-cold atoms,^[62] or quark-gluon plasmas.^[63,64]

ACKNOWLEDGEMENTS

We acknowledge stimulating discussions with A. Filinov during the early stages of our research. This work has been supported by the Deutsche Forschungsgemeinschaft via project BO1366-10/2 and by the Norddeutscher Verbund für Hoch- und Höchstleistungsrechnen (HLRN) via grant shp00015 for CPU time.

REFERENCES

- [1] D. Saumon, W. B. Hubbard, G. Chabrier, H. M. van Horn, *Astrophys. J.* **1992**, *391*, 827.
- [2] W. B. Hubbard, T. Guillot, J. I. Lunine, A. Burrows, D. Saumon, M. S. Marley, R. S. Freedman, *Phys. Plasmas* **1997**, *4*, 2011.
- [3] J. Vorberger, I. Tamblyn, B. Militzer, S. A. Bonev, *Phys. Rev. B* **2007**, *75*, 024206.
- [4] B. Militzer, W. B. Hubbard, J. Vorberger, I. Tamblyn, S. A. Bonev, *Astrophys. J. Lett.* **2008**, *688*, L45.
- [5] M. D. Knudson, M. P. Desjarlais, R. W. Lemke, T. R. Mattsson, M. French, N. Nettelmann, R. Redmer, *Phys. Rev. Lett.* **2012**, *108*, 091102.
- [6] F. Soubiran, B. Militzer, K. P. Driver, S. Zhang, *Phys. Plasmas* **2017**, *24*, 041401.
- [7] M. Schöttler, R. Redmer, *Phys. Rev. Lett.* **2018**, *120*, 115703.
- [8] S. Mukherjee, F. Libisch, N. Large, O. Neumann, L. V. Brown, J. Cheng, J. Britt Lassiter, E. A. Carter, P. Nordlander, N. J. Halas, *Nano Lett.* **2013**, *13*, 240.
- [9] M. L. Brongersma, N. J. Halas, P. Nordlander, *Nat. Nanotechnol.* **2015**, *10*, 25.
- [10] R. Nora, W. Theobald, R. Betti, F. J. Marshall, D. T. Michel, W. Seka, B. Yaakobi, M. Lafon, C. Stoeckl, J. Delettrez, A. A. Solodov, A. Casner, C. Reverdin, X. Ribeyre, A. Vallet, J. Peebles, F. N. Beg, M. S. Wei, *Phys. Rev. Lett.* **2015**, *114*, 045001.
- [11] P. F. Schmit, P. F. Knapp, S. B. Hansen, M. R. Gomez, K. D. Hahn, D. B. Sinars, K. J. Peterson, S. A. Slutz, A. B. Sefkow, T. J. Awe, E. Harding, C. A. Jennings, G. A. Chandler, G. W. Cooper, M. E. Cuneo, M. Geissel, A. J. Harvey-Thompson, M. C. Herrmann, M. H. Hess, O. Johns, D. C. Lampa, M. R. Martin, R. D. McBride, J. L. Porter, G. K. Robertson, G. A. Rochau, D. C. Rovang, C. L. Ruiz, M. E. Savage, I. C. Smith, W. A. Stygar, R. A. Vesey, *Phys. Rev. Lett.* **2014**, *113*, 155004.
- [12] A. L. Kritcher, T. Döppner, C. Fortmann, T. Ma, O. L. Landen, R. Wallace, S. H. Glenzer, *Phys. Rev. Lett.* **2011**, *107*, 015002.
- [13] T. Tschentscher, C. Bressler, J. Grünert, A. Madsen, A. P. Mancuso, M. Meyer, A. Scherz, H. Sinn, U. Zastra, *Appl. Sci.* **2017**, *7*, 592.
- [14] L. B. Fletcher, H. J. Lee, T. Döppner, E. Galtier, B. Nagler, P. Heimann, C. Fortmann, S. LePape, T. Ma, M. Millot, A. Pak, D. Turnbull, D. A. Chapman, D. O. Gericke, J. Vorberger, T. White, G. Gregori, M. Wei, B. Barbrel, R. W. Falcone, C.-C. Kao, H. Nuhn, J. Welch, U. Zastra, P. Neumayer, J. B. Hastings, S. H. Glenzer, *Nat. Photonics* **2015**, *9*, 274.
- [15] P. Sperling, E. Gamboa, H. Lee, H. Chung, E. Galtier, Y. Omarbakiyeva, H. Reinholz, G. Röpke, U. Zastra, J. Hastings, L. Fletcher, S. Glenzer, *Phys. Rev. Lett.* **2015**, *115*, 115001.
- [16] E. I. Moses, R. N. Boyd, B. A. Remington, C. J. Keane, R. Al-Ayat, *Phys. Plasmas* **2009**, *16*, 041006.
- [17] B. A. Hammel, S. W. Haan, D. S. Clark, M. J. Edwards, S. H. Langer, M. M. Marinak, M. V. Patel, J. D. Salmonson, H. A. Scott, *High Energy Density Phys.* **2010**, *6*, 171.
- [18] M. F. Herman, E. J. Bruskin, B. J. Berne, *J. Chem. Phys.* **1982**, *76*, 5150.
- [19] D. M. Ceperley, *Rev. Mod. Phys.* **1995**, *67*, 279.
- [20] T. Dornheim, S. Groth, F. D. Malone, T. Schoof, T. Sjöstrom, W. M. C. Foulkes, M. Bonitz, *Phys. Plasmas* **2017**, *24*, 056303.
- [21] M. Troyer, U. J. Wiese, *Phys. Rev. Lett.* **2005**, *94*, 170201.
- [22] E. Y. Loh, J. E. Gubernatis, R. T. Scalettar, S. R. White, D. J. Scalapino, R. L. Sugar, *Phys. Rev. B* **1990**, *41*, 9301.
- [23] T. Schoof, S. Groth, J. Vorberger, M. Bonitz, *Phys. Rev. Lett.* **2015**, *115*, 130402.
- [24] T. Dornheim, S. Groth, T. Sjöstrom, F. D. Malone, W. M. C. Foulkes, M. Bonitz, *Phys. Rev. Lett.* **2016**, *117*, 156403.
- [25] S. Groth, T. Dornheim, T. Sjöstrom, F. D. Malone, W. M. C. Foulkes, M. Bonitz, *Phys. Rev. Lett.* **2017**, *119*, 135001.
- [26] T. Dornheim, S. Groth, M. Bonitz, *Phys. Rep.* **2018**, *744*, 1.
- [27] N. S. Blunt, T. W. Rogers, J. S. Spencer, W. M. Foulkes, *Phys. Rev. B* **2014**, *89*, 245124.
- [28] F. D. Malone, N. S. Blunt, J. J. Shepherd, D. K. K. Lee, J. S. Spencer, W. M. C. Foulkes, *J. Chem. Phys.* **2015**, *143*, 044116.
- [29] F. D. Malone, N. S. Blunt, E. W. Brown, D. K. K. Lee, J. S. Spencer, W. M. C. Foulkes, J. J. Shepherd, *Phys. Rev. Lett.* **2016**, *117*, 115701.
- [30] N. S. Blunt, A. Alavi, G. H. Booth, *Phys. Rev. Lett.* **2015**, *115*, 050603.
- [31] J. Claes, B. K. Clark, *Phys. Rev. B* **2017**, *95*, 205109.
- [32] Y. Liu, M. Cho, B. Rubenstein **2018**, *14*, 4722.
- [33] S. A. Chin, *Phys. Rev. E* **2015**, *91*, 031301(R).
- [34] T. Dornheim, S. Groth, A. Filinov, M. Bonitz, *New J. Phys.* **2015**, *17*, 073017.
- [35] T. Dornheim, T. Schoof, S. Groth, A. Filinov, M. Bonitz, *J. Chem. Phys.* **2015**, *143*, 204101.
- [36] T. Dornheim, S. Groth, T. Schoof, C. Hann, M. Bonitz, *Phys. Rev. B* **2016**, *93*, 205134.
- [37] S. Groth, T. Schoof, T. Dornheim, M. Bonitz, *Phys. Rev. B* **2016**, *93*, 085102.

- [38] M. Takahashi, M. Imada, *J. Physical Soc. Japan* **1984**, 53, 963.
- [39] V. S. Filinov, M. Bonitz, V. E. Fortov, W. Ebeling, P. Levashov, M. Schlanges, *Contrib. Plasma Physics* **2004**, 44, 388.
- [40] A. P. Lyubartsev, *J. Phys. A: Math. Gen.* **2005**, 38, 6659.
- [41] S. A. Chin, C. R. Chen, *J. Chem. Phys.* **2002**, 117, 1409.
- [42] K. Sakkos, J. Casulleras, J. Boronat, *J. Chem. Phys.* **2009**, 130, 204109.
- [43] L. D. Fosdick, H. F. Jordan, *Phys. Rev.* **1966**, 143, 58.
- [44] H. F. Jordan, L. D. Fosdick, *Phys. Rev.* **1968**, 171, 128.
- [45] P. Sindzingre, M. L. Klein, D. M. Ceperley, *Phys. Rev. Lett.* **1989**, 63, 1601.
- [46] Y. Kwon, F. Paesani, K. Whaley, *Phys. Rev. B* **2006**, 74, 174522.
- [47] T. Dornheim, A. Filinov, M. Bonitz, *Phys. Rev. B* **2015**, 91, 054503.
- [48] S. Saccani, S. Moroni, M. Boninsegni, *Phys. Rev. Lett.* **2012**, 108, 175301.
- [49] A. Filinov, M. Bonitz, *Phys. Rev. A* **2012**, 86, 043628.
- [50] T. Dornheim, S. Groth, J. Vorberger, M. Bonitz, *Phys. Rev. Lett.*, **2018**, 121, 255001.
- [51] A. V. Filinov, M. Bonitz, Y. E. Lozovik, *Phys. Rev. Lett.* **2001**, 86, 3851.
- [52] B. K. Clark, M. Casula, D. M. Ceperley, *Phys. Rev. Lett.* **2009**, 103, 055701.
- [53] T. Dornheim, H. Thomsen, P. Ludwig, A. Filinov, M. Bonitz, *Contrib. Plasma Physics* **2016**, 56, 371.
- [54] T. Dornheim, S. Groth, M. Bonitz, *Contrib. Plasma Physics* **2017**, 57, 468.
- [55] M. Boninsegni, N. Prokof'ev, B. Svistunov, *Phys. Rev. Lett.* **2006**, 96, 070601.
- [56] M. Boninsegni, N. V. Prokof'ev, B. V. Svistunov, *Phys. Rev. E* **2006**, 74, 036701.
- [57] H. De Raedt, B. De Raedt, *Phys. Rev. A* **1983**, 28, 3575.
- [58] N. Metropolis, A. W. Rosenbluth, M. N. Rosenbluth, A. H. Teller, E. Teller, *J. Chem. Phys.* **1953**, 21, 1087.
- [59] R. Egger, W. Häusler, C. H. Mak, H. Grabert, *Phys. Rev. Lett.* **1999**, 82, 3320.
- [60] S. M. Reimann, M. Manninen, *Rev. Mod. Phys.* **2002**, 74, 1283.
- [61] I. Kylänpää, E. Räsänen, *Phys. Rev. B* **2017**, 96, 205445.
- [62] C. Chkravarty, *Int. Rev. Phys. Chem.* **1997**, 16, 421.
- [63] V. S. Filinov, Y. B. Ivanov, V. E. Fortov, M. Bonitz, P. R. Levashov, *Phys. Rev. C* **2013**, 87, 035207.
- [64] V. S. Filinov, M. Bonitz, Y. B. Ivanov, E.-M. Ilgenfritz, V. E. Fortov, *Contrib. Plasma Physics* **2015**, 55, 203.

How to cite this article: Dornheim T, Groth S, Bonitz M. Permutation blocking path integral Monte Carlo simulations of degenerate electrons at finite temperature. *Contributions to Plasma Physics* 2019;e201800157. <https://doi.org/10.1002/ctpp.201800157>